



Broadband acoustic resonance dissolution spectroscopy of natural edible salts: Visualization and interpretation for descriptive and diagnostic analysis

Pedram Shoa^{a,b,*}, Seyed Ahmad Mireei^b, Abbas Hemmat^b, Sara W. Erasmus^c, Saskia M. van Ruth^{a,c,*}

^a Wageningen Food Safety Research, Wageningen University and Research, P.O. Box 230, 6700 AE, Wageningen, the Netherlands

^b Department of Biosystems Engineering, College of Agriculture, Isfahan University of Technology, Isfahan 84156-83111, Iran

^c Food Quality and Design Group, Wageningen University and Research, P.O. Box 17, 6700 AA, Wageningen, the Netherlands

ARTICLE INFO

Keywords:

Acoustics
BARDS
Composition
Morphology
Salt
T-distributed stochastic neighbor embedding

ABSTRACT

Broadband acoustic resonance dissolution spectroscopy (BARDS) has been recently introduced as a low-cost method for the analysis of powdered materials. In this study, ten Iranian natural table salts, each separated into five particle size fractions, were analyzed with BARDS. The compositions and crystalline structure of samples were investigated with inductively coupled plasma optical emission spectroscopy, flame photometry, and X-ray diffraction methods. Moreover, different linear and nonlinear dimensionality reduction methods were used to visualize the ten salt types. The analyses revealed the presence of halite, sylvite, and anhydrite in the rock salts, and halite, bischofite, and periclase in the sea salts. Subjecting bubble volume spectra to nonlinear dimensionality reduction using the t-distributed stochastic neighbor embedding algorithm, the salts were clearly distinguished in a two-dimensional space with the distances and positions relative to their composition, crystalline structure, and particle morphology. The results of this study provide a roadmap toward unraveling the underlying mechanisms behind the BARDS spectra for further applications in characterizing natural edible salts.

1. Introduction

Salt is one of the main powdered food materials used as a preservative, stabilizer, texture, and taste enhancer (Lee et al., 2014). Table salts can be categorized into refined and unrefined products. Refined salt is purified sodium chloride with chemical treatments such as sulfuric acid or chlorine which may contain anti-caking agents and may be iodized. The unrefined salts exist in two types, rock salts and sea salts. Rock table salts are directly extracted from salt mines, crushed, and packed for use, whereas sea salts are produced from the evaporation of seawater or the brine of salt lakes (Lee et al., 2016). It is noteworthy that salt ions in seawater are mainly originated from leaching the land or volcanic activations at the seafloor (US Department of Commerce, n.d.). Hence, both categories of unrefined salts contain a significant amount of trace elements other than sodium (Na) and chloride (Cl), such as magnesium (Mg), potassium (K), or calcium (Ca) (González et al., 2015). The type and the percentage of these trace elements can define the quality or the geographical origin of the salt (Tan et al., 2012). Thus

quantitative analyses such as inductively coupled plasma (ICP) spectroscopy methods are usually applied for the determination of trace elements in unrefined salts (González et al., 2015; Hwang et al., 2016). X-ray diffraction (XRD) can also be used as a crystallographic method for delineating the molecule structure of constitutive salt crystals (Karavoltsov et al., 2020). Since the sample preparation for these reference analyses, is labor-intensive and time-consuming, and the experimental costs of both methods (ICP and XRD) are remarkably high, cost-efficient and rapid screening methods are proposed for determining the elemental quality or the geographical origin of unrefined salts.

Near-infrared (NIR) spectroscopy in diffuse reflectance mode has been successfully applied to discriminate sea salts, according to their quality (traditional vs. flower of salt - 'fleur de sel') and geographical origin, in conjunction with partial least square discriminant analysis (PLS-DA) (Galvis-Sánchez et al., 2011). The concentration of K and Mg varied between salts in different geographical origins, while the concentration of Ca distinguished the traditional sea salt from the flower of salt. In a follow-up study, PLS regression (PLSR) was applied to the NIR

* Corresponding authors at: Wageningen Food Safety Research, Wageningen University and Research, P.O. Box 230, 6700 AE, Wageningen, the Netherlands.

E-mail addresses: pedram.shoa@ag.iut.ac.ir (P. Shoa), saskia.vanruth@wur.nl (S.M. van Ruth).

<https://doi.org/10.1016/j.jfca.2022.104722>

Received 17 December 2021; Received in revised form 5 June 2022; Accepted 28 June 2022

Available online 30 June 2022

0889-1575/© 2022 The Authors. Published by Elsevier Inc. This is an open access article under the CC BY license (<http://creativecommons.org/licenses/by/4.0/>).

and mid-infrared (MIR) spectroscopic data to predict the percentage of the trace elements in sea salt and brine samples (Galvis-Sánchez et al., 2013).

In another study, laser-induced breakdown spectroscopy (LIBS) was used for the classification of sea salts based on their geographical origin. It was reported that K, Mg, Ca, and aluminum (Al) concentrations varied with the provenance of salts. The concentration of the mentioned elements was consistent with the relative intensities of the peaks observed in the LIBS spectra. By serving the LIBS spectra as the inputs of PLS-DA models, different salt samples were classified (Lee et al., 2014; Tan et al., 2012). In a follow-up study, the classification accuracy was improved using soft independent modeling of class analogy (SIMCA) due to its higher efficiency with a large number of sample classes (Lee et al., 2017).

During the last decade, broadband acoustic resonance dissolution spectroscopy (BARDS) has been proposed for the qualitative and quantitative analysis of powders (Fitzpatrick et al., 2012). In this method, the acoustic profile of a powdered sample is recorded during the dissolution in its solvent such as pure water. The profile is the changes in sound frequency passing through the solution in a vessel during the dissolution process. The frequency change is due to the entrance, growth/generation, and subsequent elimination of minute air bubbles. Entrained bubbles are originated from the collision of solid particles with the liquid surface and the entrapment of air between solute particles. However, the driving force for the growth/generation of the bubbles in the solution during the dissolution process is the reduction of gas solubility in the liquid solvent as the consequence of dissolving a solid solute, which is known as "The hot chocolate effect" (Crawford, 1982; Fitzpatrick et al., 2013, 2012). During the dissolution of a substance in its liquid solvent, the solution gets oversaturated by those amounts of gas, which have been dissolved in the solvent, before the addition of the solute. The gas oversaturated liquid will move toward the steady-state condition by nucleating air bubbles or growing the entrained bubbles. Those air bubbles can impressively reduce compressibility and insignificantly lessen the density of the liquid media, hence reducing the velocity of sound. As the wavelength of the sound is equal to its velocity divided by its frequency in a closed-end sound tube, the sound velocity is proportional to its frequency at each wavelength. Measuring the changes of sound frequency passing through the pure solvent and the bubble-filled solution makes it possible to track the bubble volume during the dissolution process.

In a previous study, the effect of salt's composition and particle morphology on the acoustic profile has been reported using natural salts as well as the artificial mixture of analytical grade edible salts, including NaCl, KCl, and MgCl₂ (van Ruth et al., 2019). A more comprehensive study on the mixture of analytical grade edible salts revealed the responsible physicochemical characteristics of a sample to be responsible for the changes in the acoustic spectra. The identified characteristics were the dissolution rate and gas solubility reduction of the powder besides the viscosity and surface tension of the solution. In this study, the composition of the salt mixtures was effectively predicted using BARDS spectra and multivariate regression methods (Shoa et al., 2021). Despite the previous studies, a thorough comprehension of the effect of compositional differences in combination with crystalline structure characteristics on the sound signatures of natural salts generated by BARDS will help to elucidate the underlying mechanisms that determine these sound signatures. This requires analysis of natural salts with BARDS but also characterization of the salt's composition and crystalline structures with other analytical techniques.

To relate features and interpret these high dimensional spectral data, an important way forward is to visualize spectral data with unsupervised dimensionality reduction (DR) methods (Bishop, 2006). Unsupervised DR methods could be categorized into linear and non-linear, random projection, and manifold-based methods. It was reported that manifold-based methods retain the local data structures and deal well with the non-linearity of the data in a more effective manner (Anowar

et al., 2021; Sorzano et al., 2014). It is noteworthy that the global and local structures of data should be preserved after mapping.

The goal of this study is to examine the ability of the BARDS data obtained from various rock and sea salts, in combination with different unsupervised DR methods to relate the sound signatures to the differences in composition, crystalline structure, and the particle morphology of salts. The interpretation of spectral data in their raw form as well as in the reduced space, regarding the crystalline structure and the chemical composition of the natural edible salts, could be considered as the novelty aspects of this study.

2. Materials and methods

2.1. Salt samples

Samples from ten different types of rock (seven) and sea (three) salts were collected from Iranian salt producers. The ten salt types, shown in Fig. 1, originated from Iranian salt mines and lakes. Due to the hygroscopic nature of the unrefined salts, all samples were oven-dried at 103°C before the analysis. Salts were ground using a commercial coffee grinder (Tristar KM-2270 Tristar, Smartwares Group, Tilburg, the Netherlands). For the BARDS measurements, the ground salts were subsequently passed through different sieves to obtain five different particle size classes with the following codes and the corresponding particle size ranges in parenthesis: A (500–650 µm), B (350–500 µm), C (250–350 µm), D (150–250 µm), and E (63–150 µm). A total number of 50 salt samples were analyzed with BARDS. The samples were kept in plastic bottles to prevent further reabsorbing ambient humidity.

2.2. Elemental analysis

About 50 g of each salt type in intact form was finely ground, to obtain a homogeneous sample for analysis. One gram sample from each salt type (ground) was dissolved in 100 mL of 1 % HNO₃ (using ultra-pure water R~18 MΩ) and shaken. Subsequent dilutions of 10, 10², 10³, 10⁴, and 10⁵ times were prepared. The concentration of Al, B, Ba, Be, Bi, Ca, Cd, Co, Cr, Cu, Fe, Ga, K, Li, Mg, Mn, Na, Ni, Pb, Se, Sr, Te, Ti, and Zn were determined for each salt sample in the linear five sets of dilutions, using ICP optical emission spectroscopy (ICP-OES) (Optima 7300DV, PerkinElmer Inc., USA). Additional analysis for highly concentrated elements of Na and K was performed using the flame photometry-based method described in a national regulation of the Netherlands (Landbouwkwaliteitsregeling Annex IX, 1994; BWB XP Flame Photometer, Instrument Solutions Benelux, Nieuwegein, the Netherlands). Detailed descriptions of the photometry method are available in a previous study (van Ruth et al., 2019). All samples were measured in duplicates.

2.3. X-ray diffraction analysis

To determine the crystalline structure of the salt samples, X-ray diffraction (XRD) analysis was performed using an AW-DX 300 (Asenware, China) diffractometer, with Cu Kα radiation (1.54060 Å, 40 kV, 30 mA), an incidence angle of 1°, recording in a 2θ range between 10° to 90° with a step size of 0.05°, and measuring time per step of 1 s. About one gram of each salt type from the finely ground salts (prepared previously for ICP-OES analysis) was analyzed.

2.4. Broadband acoustic resonance dissolution spectroscopy

A broadband acoustic resonance dissolution spectrometer (BARDS Acoustic Science Labs, Cork, Ireland) was used to obtain the acoustic profiles of the salt samples (Fig. 2). This spectrometer has a dissolution vessel made of borosilicate, suitable for 25 mL solvent which was demineralized water in this study. The sound was generated by the means of a magnetic stirrer, rotating off-set at the speed of 300 rpm, exciting the vessel's wall. The acoustic sensor was a uni-directional,

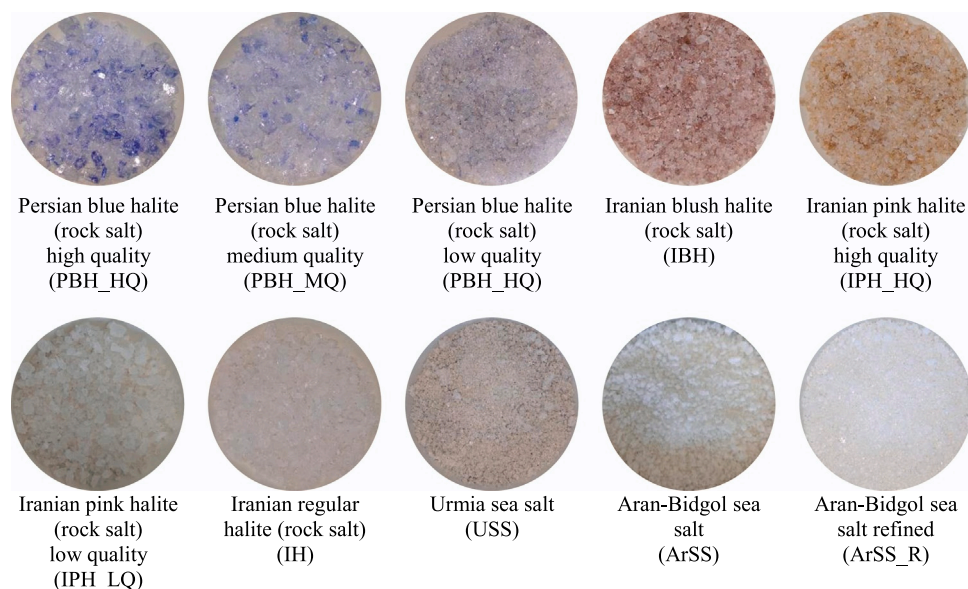


Fig. 1. The ten different Iranian natural table salts, used in this study. The brief name related to each salt is used in further sections. The quality grades were determined by the visual inspections by the producers.

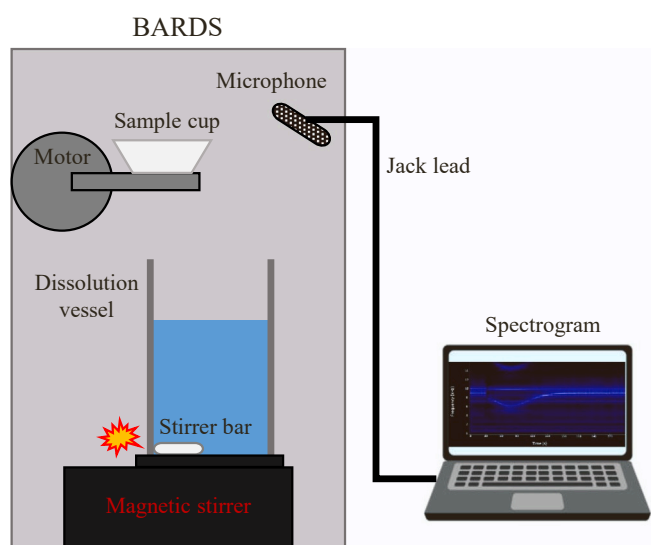


Fig. 2. Schematic overview of the data acquisition system for broadband acoustic resonance dissolution spectroscopy (BARDS).

cardio design, condenser microphone (Sony ECM-CS10), sensible in the frequency range of 100 Hz to 16 kHz. The analog output of the microphone was digitized using a sound card at a 44.1 kHz sampling rate which was suitable for the reconstruction of acoustic waves up to 22.1 kHz frequencies, covering the microphone sensitivity range (NYQUIST, 1928). The digital signal was transformed from the amplitude-time into the power-frequency-time space using a short-term Fourier transform (STFT) by performing a fast Fourier transform (FFT) on each window of 16384 data points. The output was a spectrogram in which the color intensity represents the power of the signal at each frequency-time data.

Acoustic signals were recorded for 30 s to detect the resonance frequencies of the system in absence of bubbles. At the 30 s time-point, 0.8 g of the solute was automatically added to the vessel (with 25 mL of demineralized water) using a sample cap and an electrical motor. One of the resonance frequency lines, which was continuous during the first 30 s of the measurement, dropped to a lower frequency after the addi-

tion of the salt sample. This frequency is related to those sound waves passing through the liquid media of the system and reduced by the appearance of entrained bubbles. Frequency reduction continued until the 300 s, which was found sufficient to assure that all bubbles liberate from the solution and the detected frequency curve reached the same frequency of the first 30 s. This curve is the lowest variable frequency-time course, called the fundamental curve (FC). Fifty time-points were pre-defined for each spectrogram. The relative frequency for each time-point was manually selected from visually detected FC and saved in an Excel file. The frequency spectra were transformed into the bubble volume ones using Eq. (1):

$$\frac{freq}{freq_w} = \sqrt{1 + 1.49 \times 10^4 f_a} \quad (1)$$

where f_a is the volume fraction of bubbles in the liquid, $freq_w$ is the frequency of sound in water with no bubbles (frequency of the first 30 s) and $freq$ is the frequency of sound in the bubble-filled water (frequency after 30 s) (Crawford, 1982; Del Grosso and Mader, 1972).

Savitsky-Golay derivative transformation with the number of three smoothing points was then applied to the bubble volume (BV) spectra to calculate the bubble volume rate (BVR) spectra (Savitsky and Golay, 1964).

Measurements were conducted in a conditioned laboratory at the stable room temperature of 22°C and an atmospheric pressure of ~1 atm, without any heating or cooling of the solvent. Before performing the experiments, gas saturation was stabilized in the solvent using vigorous agitation by shaking the solvent bottle for 60 s and then allowing it to rest for more than 30 min. All samples were analyzed in triplicate, hence a total of 150 measurements were performed.

2.5. Particle size measurements

To determine the size distribution of salt particles, a laser diffraction analyzer (Mastersizer 3000, Malvern Instruments, Malvern, UK) with Aero S dry powder dispersion accessory was utilized. Particles were dispersed and traveled through the detection cell by means of airflow with the settings of 2 bar pressure, 3 mm of hopper gap, and a feed rate of 20 % using a vibrational feeder. The calculations were based on the theory of diffraction by Fraunhofer. In this method, the intensity of scattered light by a particle is directly proportional to its size (Li et al.,

2019). For modeling, particle type was also selected as a non-spherical particle with the Fraunhofer approximation. Measurements were recorded once the obscuration was between 0.5 % and 6.0 %. Similar to previous studies, the particle size characteristics for salt samples in each particle size class, were recorded as D_x (50), the median diameter (van Ruth et al., 2019). The average of triplicate measurements was demonstrated in further spectral interpretation and visualization analysis.

2.6. Data visualization

Three different data sets related to spectral types of FC, BV, and BVR were created. Samples and variables were arranged along the first and second dimensions of a matrix, respectively. The matrix was then mean-centered and scaled according to the standard deviation of each variable, named X. For a better interpretation of spectral data, five different DR methods were applied to the X including PCA, non-negative matrix factorization (NMF), isometric mapping (Isomap), uniform manifold approximation and projection (UMAP), and t-distributed stochastic neighbor embedding (t-SNE). The PCA linearly projects the data from initial variables into lower orthogonal dimensions, each presenting the highest possible variation that exists in data. This method was performed using the nonlinear iterative partial least squares (NIPALS) algorithm and full cross-validation (Wold et al., 1987). The NMF also linearly maps the original high dimensional variable space into a low one. The original data should only have positive amounts and the algorithm produces also positive sample values in the new space. Hence, the method represents the data as additive combinations of different parts, which is way more interpretable than the PCA (Guimet et al., 2006). It is assumed that X could be decomposed into two matrices of basis functions (W) and encodings (H). Using multiplicative update rules, the algorithm minimizes the squared Frobenius norm F (extension of Euclidean norm to matrices) as the distance between X and W.H (Lee and Seung, 1999):

$$F = \sum_i \sum_j X_{ij} \log(WH)_{ij} - (WH)_{ij} \quad (2)$$

The Isomap is a nonlinear manifold and neighborhood graph-based DR method. Like the multi-dimensional scaling method, it aims to maintain the pairwise distances between data points in embedded space as it was in the original one. The Isomap calculates the pairwise geodesic distances between data points to generate a neighborhood graph, able to capture the nonlinear manifold patterns in the data despite the classic Euclidean method. By the means of Floyd's or Dijkstra's algorithms, the shortest path between each pair of data in the neighborhood graph will be found to approximate the geodesic distance between them. A matrix of these pairwise geodesic distances as d^G is created for all data points. The algorithm converts the distance matrix into a kernel matrix K using a centering matrix of $H = I - 1/n(ee^T)$:

$$K = H.d_G.H \quad (3)$$

where n is the number of data points, I is the identity matrix and e is a column vector of ones. By Eigen decomposition of K ($K \rightarrow B.D.B^T$), a diagonal matrix D will represent Eigenvalues and B the corresponding Eigenvectors of K . As the goal was data visualization in two dimensions top two Eigenvalues and their vectors were served and the rest of them were removed ($D \rightarrow \hat{D}_{2 \times 2}$ and $B \rightarrow \hat{B}_{n \times 2}$). Hence the data points in the new space will be calculated as:

$$Y = \hat{D}^{-1/2} \cdot \hat{B}^T \quad (4)$$

The t-SNE is a non-linear dimensionality reduction algorithm categorized in manifold learning methods to visualize high dimensional data in the space of two or three embedded dimensions. It reserves the local and global structures of the high dimensional data (X) in the projected

one (Y) by the following procedure. The algorithm first calculates the joint probability of each pair of data points in the high dimensional data (x_i and x_j) of N objects as p_{ij} which is considered as the similarity between the pair of objects:

$$p_{ij} = \frac{p_{ji} + p_{ij}}{2N} \quad (5)$$

$p_{i=j}$ refers to the conditional probability of i^{th} object picking the j^{th} one as its neighborhood, proportioned to their probability density following a Gaussian distribution centered at x_i and variance of σ :

$$p_{ji} = \frac{\exp(-\|x_i - x_j\|^2 / 2\sigma_i^2)}{\sum_{k \neq i} (\exp(-\|x_i - x_k\|^2 / 2\sigma_i^2))} \quad (6)$$

a perplexity should be determined by the user as the number of neighbors included in the Gaussian kernel and calculates its bandwidth σ , accordingly. The second step is to calculate the similarities between pairs of data points in the projected space Y. Instead of Gaussian, it uses a Student's t-distribution with one degree of freedom (same as a Cauchy distribution) with a heavy tail to handle modeling far distances.

$$q_{ij} = \frac{(1 + \|y_i - y_j\|^2)^{-1}}{\sum_{k \neq i} (1 + \|y_i - y_k\|^2)^{-1}} \quad (7)$$

The similarities (joint probabilities P and Q) should be maintained during the projection from X into Y space. Hence the algorithm uses the Kullback-Leibler divergence (relative entropy) which measures the difference of one probability distribution from another as a loss function:

$$KL(P||Q) = \sum_i \sum_j p_{ij} \log \frac{p_{ij}}{q_{ij}} \quad (8)$$

Herein an optimization problem of minimizing the above loss function could be solved using the gradient descent approach. The result is the Y space, visualizing the similarities of objects in X space (Hinton and Roweis, 2002; Van der Maaten and Hinton, 2008).

The UMAP is also a non-linear dimensionality reduction method, which could be considered as an updated version of t-SNE. By the means of local manifold approximations and local fuzzy simplicial set representations, the algorithm creates a topological representation of high and low dimensional data sets. The optimization aims to minimize the distance between two topological representations (fuzzy sets). Using the stochastic gradient descent method minimizes the fuzzy set cross-entropy (Eq. 5) as loss function instead of Kullback-Leibler divergence used by t-SNE, helping the algorithm to retain the global structure of the data more efficiently.

$$C = \sum_{i \neq j} \left(\mu_{ij} \log \frac{\mu_{ij}}{v_{ij}} + (1 - v_{ij}) \log \frac{(1 - \mu_{ij})}{(1 - v_{ij})} \right) \quad (9)$$

where μ and v are fuzzy simplicial similarities of the high and low dimensional spaces, respectively (McInnes et al., 2018).

All data transformations were implemented with Python 3.7 and the following toolboxes including scikit-learn and UMAP (Harris et al., 2020; McInnes et al., 2018; Pedregosa et al., 2011).

3. Results and discussion

3.1. Elemental analysis of salts

The elemental concentrations and detected compounds of the ten salt types are shown in Table 1. For highly concentrated elements of Na and K, the concentrations were measured with flame photometry and are reported in Table 2. It was observed that K presented in all salt samples but its concentration was remarkably higher in the four rock salts, namely PBH_HQ, PBH_LQ, IPH_LQ, and IH. Regarding the XRD analysis,

Table 1

Elemental and composition results of each salt, reported from inductively coupled plasma optical emission spectroscopy (ICP-OES) and X-ray diffraction analyses, respectively.

Salt type	Elements ^a						Compounds
	Na (mg/g)	K (mg/g)	Mg (mg/g)	Ca (mg/g)	Al (mg/g)	Fe (mg/g)	
PBH_HQ	345 ± 9	32.67 ± 0.33	0.41 ± 0.04	0.45 ± 0.03	N.D.	N.D. ^b	Halite ^c Sylvite ^d
PBH_MQ	366 ± 15	1.06 ± 0.12	0.05 ± 0.00	0.10 ± 0.03	N.D.	N.D.	Halite
PBH_LQ	320 ± 1	58.01 ± 1.10	0.20 ± 0.09	1.01 ± 0.10	0.05 ± 0.00	0.02 ± 0.00	Halite, Sylvite, Anhydrite ^e
IBH	350 ± 22	0.90 ± 0.05	0.25 ± 0.08	2.6 ± 0.88	0.1 ± 0.02	0.02 ± 0.00	Halite, Anhydrite
IPH_HQ	317 ± 11	0.65 ± 0.09	1.71 ± 0.10	2.24 ± 0.00	0.02 ± 0.00	0.02 ± 0.00	Halite, Anhydrite
IPH_LQ	314 ± 1	65.10 ± 1.30	0.72 ± 0.03	2.12 ± 0.00	0.01 ± 0.00	0.01 ± 0.00	Halite, Sylvite, Anhydrite
IH	313 ± 8	59.10 ± 0.20	0.40 ± 0.01	0.75 ± 0.20	0.01 ± 0.00	N.D.	Halite, Sylvite
USS	271 ± 6	2.78 ± 0.09	5.46 ± 1.76	0.66 ± 0.02	0.02 ± 0.00	N.D.	Halite, Bischofite ^f
ArSS	343 ± 11	1.38 ± 0.33	3.12 ± 0.78	1.33 ± 0.09	N.D.	N.D.	Halite, Periclase ^g Bischofite
ArSS_R	333 ± 1	1.17 ± 0.47	4.76 ± 0.38	0.25 ± 0.02	0.04 ± 0.01	N.D.	Halite, Bischofite

^a Values were averages, calculated over duplicate measurements and wavelength lines.

^b (N.D.) non-detected.

^c NaCl,

^d KCl,

^e CaSO₄,

^f MgCl₂ (H₂O)₆,

^g MgO: (Na) sodium; (K) potassium; (Mg) magnesium; (Ca) calcium; (Al) aluminum; (Fe) iron.

Table 2

The percentage of sodium chloride (NaCl) and potassium chloride (KCl), calculated from the results of flame photometry, assuming all the soluble sodium and potassium are in their chloride form. Values are the average of two prepared solutions from each salt at each particle size class.

Salt type	NaCl (%)			KCl (%)		
	Mean	STD	CV %	Mean	STD	CV %
PBH_HQ	83.0	3.8	4.6	5.2	0.5	9.9
PBH_MQ	85.6	3.9	4.6	N.D.	–	–
PBH_LQ	76.4	3.0	3.9	10.3	1.2	12.2
IBH	82.5	1.4	1.6	N.D.	–	–
IPH_HQ	79.5	3.7	4.7	N.D.	–	–
IPH_LQ	72.3	4.3	5.9	11.3	1.3	12.1
IH	70.6	6.4	9.0	11.6	0.4	3.9
USS	83.4	0.8	0.9	N.D.	–	–
ArSS	81.2	0.7	0.9	N.D.	–	–
ArSS_R	79.9	2.3	2.8	N.D.	–	–
Total	79.4	4.6	5.9	9.6	2.6	26.6

N.D. stands for non-detected and STD for standard deviation. The coefficient of variation (CV) for analysis of NaCl was 0.2 % and for KCl was 0.3 %.

halite and sylvite were detected in these four rock salts, which are chloride crystalline forms of Na and K. Thus, the percentage of NaCl and KCl were calculated from the concentrations of Na and K. The PBH_HQ salt had the lowest KCl concentration (5.2 %), while the highest KCl concentrations (11.6 % and 11.3 %, respectively) were determined for IPH_LQ and IH, followed by PBH_LQ (10.3 %). In fact, the KCl concentration is a key characteristic of Persian blue halite (PBH). Among the three quality levels of PBH that were visually evaluated by the producers, the medium quality had a very low KCl concentration. Meanwhile, the lowest quality of PBH (PBH_LQ) had the highest KCl concentration among three quality levels, revealing the necessity of a low-cost quality control method for recognizing samples according to their chemical composition.

Mg is another important element for the evaluation of natural salts, as presented in all salt samples of this study. The highest concentration of Mg was found in sea salts. For the rock salt samples, XRD was not able to recognize any compound containing Mg. Bischofite was detected by XRD in three sea salts which is the hydrated form of magnesium chloride (MgCl₂). In the ArSS, XRD also detected periclase, the oxide form of Mg (MgO). Among the three sea salts, USS had the highest amount of MgCl₂. Between the two Aran sea salts, ArSS was expected to have less Mg in chloride form when compared to ArSS_R, due to the presence of MgO.

Iron (Fe) was also present in PBH_LQ, IBH, IPH_HQ, and IPH_LQ, in

which a few orange streaks were obvious on the halite crystals. Those streaks were likely related to the oxide form of Fe. The Fe compounds were not detected by XRD analysis. Calcium was presented at every salt sample. Anhydrite (CaSO₄) was detected by XRD in PBH_LQ, IBH, IPH_HQ, and IPH_LQ. Almost all rock and sea salts contained Al but the highest amount of 0.1 mg per gram of salt was recorded for IBH.

3.2. Spectral interpretation

Fig. 3 represents a) the FC, b) the BV, and c) the BVR spectra of the ten salt types in the particle size class B (350–500 μm). At the entrance response point (ERP), i.e., the first data point after powder introduction to the solvent (33 s), the frequency (F_{ERP}) of rock salts (PBH_HQ, PBH_MQ, PBH_LQ, IBH, IPH_HQ, IPH_LQ, and IH) were very similar to each other (Fig. 3a). F_{ERP} of the sea salts (USS, ArSS, and ArSS_R) was remarkably lower than those of the rock salts. The lower F_{ERP} at the same particle size range represents the higher powder ability of bubble formation at the early stages of the dissolution (Fig. 2). The presence of MgCl₂ in the sea salts (Table 1) may be the cause of the lower frequency (higher bubble volume) at early seconds after the introduction of solute to the solvent. It has been stated that the causes of lower F_{ERP} between two powders in the same particle size range are due to a higher total dissolution rate and higher ability of the powder to reduce the gas solubility in a liquid solvent. It has been found that MgCl₂ has a higher dissolution rate and more ability to reduce the gas solubility in the solvent, compared to NaCl and KCl (Shoa et al., 2021).

For the time-points after the ERP, the sea salts had spectra with a noticeable lower frequency and higher bubble volume compared to the rock salts. A previous study reported that the presence of MgCl₂ in the salt mixture powders considerably increased bubble formation (Shoa et al., 2021). Magnesium chloride has a high ability to reduce the gas solubility of the solvent, mainly due to its negative dissolution enthalpy. The spectrum with the highest bubble volume (lowest frequency) referred to USS with the highest Mg content in the form of bischofite (MgCl₂ (H₂O)₆). The second and third spectra with the highest bubble volume referred to ArSS_R with a slightly lower Mg content in the same form of bischofite and then the ArSS, with the lowest Mg content among the sea salts. In this salt, Mg was not only in the form of bischofite but also appeared as periclase (MgO). Among the seven types of rock salts, the IPH_HQ had the highest bubble volume (lowest frequency) at time-points after ERP, especially near the overall minimum point of the FC spectrum (F_{min}). The IPH_HQ salt had the highest Mg content among the rock salts, but the composition was not detected by the XRD. The

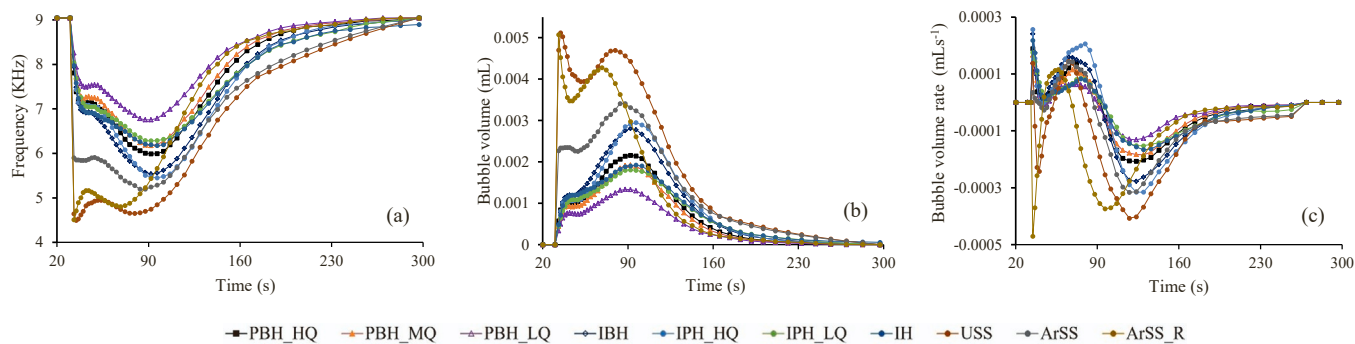


Fig. 3. The average spectra of ten Iranian natural table salt types, obtained from three measurements (particle size class B: 350–500 μm), representing (a) fundamental curve (FC), (b) bubble volume (BV), and (c) bubble volume rate (BVR). Persian blue halite high quality (PBH_HQ), Persian blue halite medium quality (PBH_MQ), Persian blue halite low quality (PBH_LQ), Iranian bluish halite (IBH), Iranian pink halite high quality (IPH_HQ), Iranian pink halite low quality (IPH_LQ), Iranian regular halite (IH), Urmia sea salt (USS), Aran-Bidgol sea salt (ArSS), Aran-Bidgol sea salt refined (ArSS_R).

PBH_LQ salt had the lowest bubble volume spectrum (highest frequency). No relationship was observed between the position of the spectra and the NaCl or KCl content of the rock salts. This finding is in line with a former study in which no correlation between the NaCl content of natural salts and the F_{min} or the time needed to reach this point (Δt) were reported (van Ruth et al., 2019).

A sinusoidal shape was obvious in the BVR spectrum of all the salt samples (Fig. 3c), except for ArSS_R. The maximum and minimum points of the sinusoidal shape temporally coincided at all the salt samples. The same sinusoidal shape was also observed in a previous study and claimed to be the fingerprint of NaCl in salt mixtures (Shoa et al., 2021). Since most salt crystals in this study were NaCl, a similar fingerprint was achieved.

3.3. Visualizing the spectral data

3.3.1. Principal component analysis overview

Fig. 4 shows the score plots of the two main principal components (PCs) derived from a) the FC, b) the BV, and c) the BVR spectra, respectively. The plots show higher discrimination between ten salt samples, for the FC and BV dataset, followed by BVR. In Fig. 4a and b, the sea salts were located far from rock salts and also from each other, especially on the horizontal axes. This is due to the effect of the MgCl_2 content on the bubble formation and hence the FC spectrum, which is obvious in Fig. 3a and b. From the left to the right of Fig. 4a and b, the sea salt samples are arranged with an increasing Mg content (bischofite). This phenomenon was also observed in a previous study on PCA score plots related to the mixtures of analytical salts (Shoa et al., 2021). The IPH_LQ salt had a high amount of Mg but was located among the other rock salts, on the left side of the PC plots, since its Mg content was not in the chloride form to have a significant effect on the gas oversaturation of the solution. By using BV spectra in Fig. 4b, the sea salts were located with more distance from the rock salts and from each other, when compared to Fig. 4a, which is related to FC spectra. In this plot, different particle sizes of each salt, which were located in smaller clusters, in comparison with the plot related to FC spectra. On the vertical axis, those samples with a lower K content (IBH and IPH_HQ) were located below the ones with higher K contents (PBH_HQ, PBH_LQ, IPH_LQ, and IH), except for PBH_MQ with a very low K content located almost at the top of the other rock salts besides the PBH_LQ (Fig. 4b). The PBH_HQ samples in different particle size classes were effectively discriminated from PBH_MQ and PBH_LQ.

3.3.2. Non-negative matrix factorization overview

Fig. 4d, e, and f depict the plots of the two main factors derived from applying NMF to FC, BV, and BVR spectra, respectively. Similar to the PCA results, the sea and rock salts were well distinguished from each other in these plots. Moreover, the plots related to FC and BV spectra

were more efficient in separating the salt types when compared to BVR. Unlike the PCA results, no relation could be observed between the location of sea salts and their Mg or K contents.

3.3.3. Isometric mapping overview

Fig. 4g, h, and i illustrate the ten salt samples in two dimensions derived from the Isomap transformation of FC, BV, and BVR spectra, respectively. Samples were distributed on plots with a three-pronged shape. The Isomap transformation of FC spectra (Fig. 4g) did not result in satisfactory discrimination of the samples, since it overlaid the sea salt ArSS_R with the PBH_LQ, one sample with a significant amount of MgCl_2 with another by an almost non-determinable amount of MgCl_2 , respectively. This is while the Isomap transformation of the BV spectra (Fig. 4h) resulted in a more effective allocation of the rock salts. At the upper prong in Fig. 4h, two salts of IBH and IPH_HQ were located with almost similar compositions (Table 2), the one with lower Na content (IPH_HQ) at the top of another with the higher one. Three salts with a considerable amount of KCl (PBH_HQ, IPH_LQ, and IH) were located on the lower prong, increasing the KCl content from the tip to the prong union upward. On the left prong, the two Persian halite salts of lower qualities were located (with non-similar compositions); these two salts were also located close together on PCA and NMF plots. At the center of Fig. 4h (not obvious in the figure), the three sea salts were located such that the USS and ArSS were overlaid and ArSS_R located on top of them. Like PCA and NMF, the Isomap transformation of BVR spectra (Fig. 4i) did not lead to promising results for the rock salts, but it effectively separated rock salt from sea salts. In this plot, a trend of MgCl_2 content is obvious between sea salts from the top to the bottom of the plot. In another study on grouping a musical loops database, Isomap outperformed the PCA, which is in line with the findings of this study (Dupont et al., 2013).

3.3.4. The *t*-distributed stochastic neighbor embedding and uniform manifold approximation and projection overview

Since the basic principles of the t-SNE and UMAP algorithms are almost similar, their plots are discussed together. Fig. 4j, k, and l show the t-SNE mapping and the Fig. 4m, n, and o illustrate the UMAP projection of FC, BV, and BVR spectral data, respectively. For the best performance of the algorithm, the perplexity in t-SNE corresponding to the number of nearest neighbors, and the number of iterations were set at five and 5000, respectively. The number of neighbors for UMAP was also set at five. The mentioned hyperparameters were found heuristically, by visually evaluating their plots.

Similar to the previously discussed methods, applying UMAP and t-SNE algorithms on BV spectral data, clustered samples with similar compositions in a more effective manner, compared to FC or BVR spectral data. The comparison of Figs. 4k and n revealed the superiority of t-SNE in clustering samples according to their salt types. In Fig. 4k, the

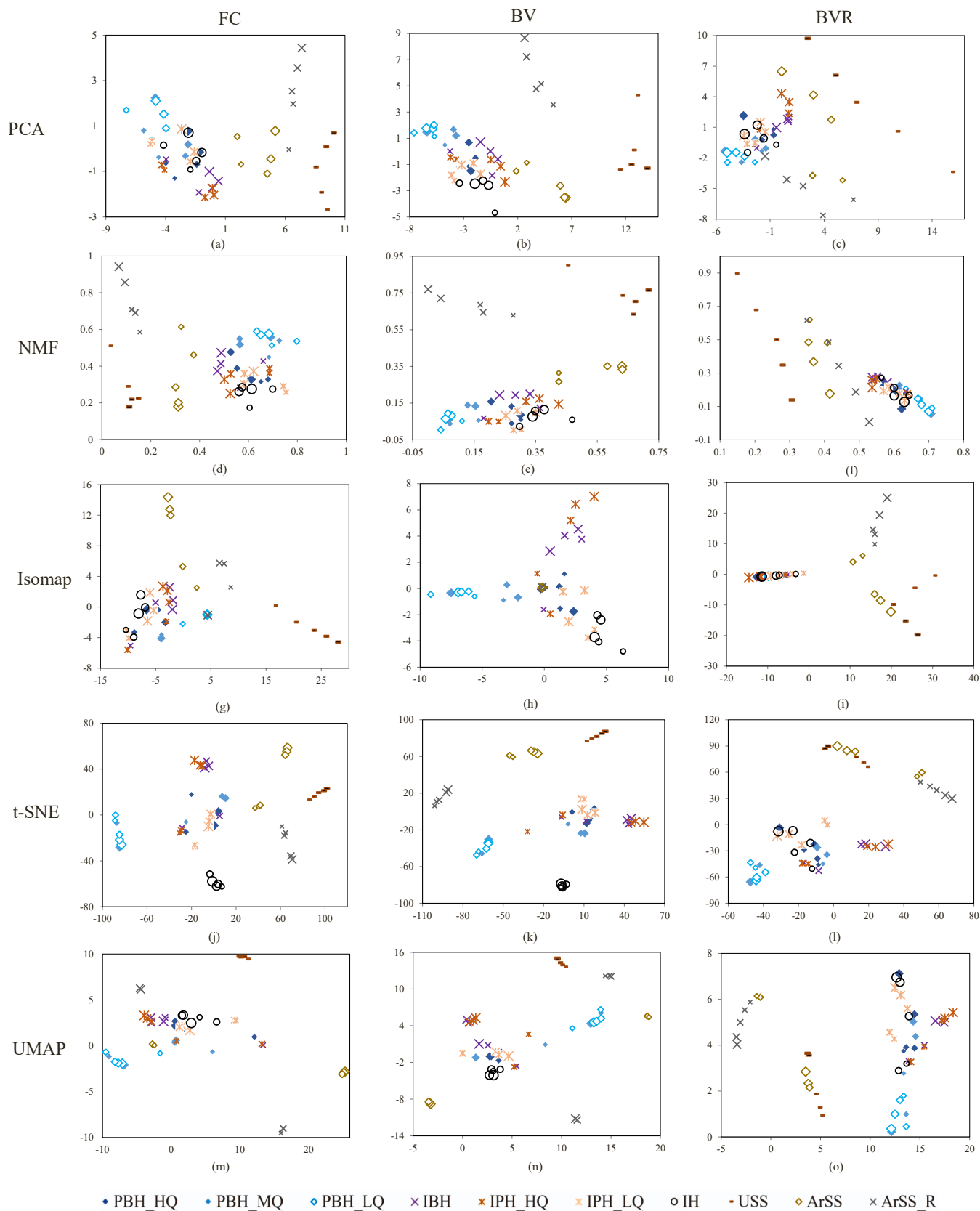


Fig. 4. The visualization of the salt samples in two dimensions by applying five dimensionality reduction methods (principal component analysis (PCA), non-negative matrix factorization (NMF), isometric mapping (Isomap), uniform manifold approximation and projection (UMAP), and t-distributed stochastic neighbor embedding (t-SNE)) on data related to three types fundamental curve (FC), bubble volume (BV), and bubble volume rate (BVR) spectra. The five sizes of the markers indicate A (500–650 μm), B (350–500 μm), C (250–350 μm), D (150–250 μm), and E (150–63 μm) particle size classes. For interpretation of the colors refer to the web version of the paper.

three sea salts were located on the upper part of the plot in relatively dense clusters, reducing their NaCl from right to the left. The positions of the sea salts were not associated with their MgCl₂ contents. At the bottom of the plot, the HI samples were grouped in a very dense cluster, having the highest KCl and lowest NaCl contents. From the right to the left of Fig. 4k, the KCl content seems to be increased. On the right side of the plot, the IPH_HQ and IBH rock salt types, with almost similar Na, Ca, and K contents (Table 2), were located close together. This allocation was similar to other DR methods, but for t-SNE the clusters of these two salts had a higher distance from others. The PBH_MQ samples with the highest NaCl and very low KCl contents did not show a dense cluster. For this sample, three particle sizes (B: 350–500 μm, and C: 250–350 μm, and D: 150–250 μm) were located close to IPH_HQ and IBH, and the two other particle sizes (A: 650–500 μm, and E: 150–63 μm) were located near the PBH_LQ samples with almost high KCl content. For most of the salts, different particle sizes made a dense small cluster in both t-SNE and UMAP algorithms, which was not observed in the results of the other DR methods. This means that these two algorithms have successfully recognized similarities in different parts of their BV spectral data manifold. In some cases, three higher particle size ranges (A: 500–650 μm, B: 350–500 μm, and C: 250–350 μm) located close together, while the others (D: 150–250 μm, and E: 150–63 μm) located far from the first three ones. This phenomenon revealed that by decreasing particle size, the inter-class variation may increase, causing a reduction in the consistency of the method. This finding is also in line with the results of a previous study, where the salt samples with finer particles dispersed on the PC score plots, far from other samples with similar compositions, but with coarser particle size classes (Shoa et al., 2021).

It seems that linear mapping of PCA was not efficient for extracting useful data from the acoustic spectra to represent the chemical differences among the salt types. This could be due to the purpose of PCA in finding the axis with the highest variation, instead of looking for the sample similarities. Similar to the PCA results, the NMF method was not able to follow the chemical differences among the samples in its visualizations and hence it could not effectively cluster the same samples. Since this method is also basically linear, the idea of an existing nonlinear structure in the data related to rock salts is getting more probable. The origin of this nonlinearity was likely the consequence of variation in particle size rather than chemical composition and crystalline structure. It could be due to the fact that they were remarkably scattered in the NMF and PCA plots, despite the similarities in the chemical composition of the different particle size classes. In the PCA or NMF results, the sea salts were not located in the same position with either rock salts or each other, while it occurred when using the Isomap method (Section 3.3.3). This indicates that the data structure of the rock salts was non-linear, while the acoustic data of sea salts were interpretable in linear projections (PCA and NMF).

A comparison of the five DR methods on the three spectral types of data (Fig. 4) revealed that the t-SNE had the best clustering performance with the cluster positions more relevant to the salts compositions in using the bubble volume spectra. The results confirmed the potential application of the BARDS spectrum with t-SNE for authenticating the natural edible salts. In fact, the position of an unknown sample relative to the authentic products in the reduced space of t-SNE using their BV spectrum could be a good index of its authenticity. These results are in accordance with another study, that utilized the acoustic features for characterizing the weld joints. They compared PCA, Isomap, and t-SNE methods and revealed that the t-SNE is more capable of exploring the samples based on their weld penetration (Wu et al., 2017). Unlike the priority of t-SNE in this study, in another research, the UMAP method showed more promising results in visualizing the infant vocalization over growth periods (Pagliarini et al., 2022). Although there was a slight difference between the explorative ability of t-SNE and UMAP in this study, the better discrimination of t-SNE between different classes of samples could be due to the more attention of this method to the local

data structures compared to UMAP.

4. Conclusions

This study provides an in-depth understanding of the relationships between the BARDS spectra and the natural edible salts characteristics, which includes salt composition, crystalline structure, and particle morphology. The time-frequency and bubble volume spectra of the salt samples were distinct and made it possible to distinguish between salts with different compositions. The MgCl₂ content had the highest influence on the acoustic spectra followed by the KCl content. The t-SNE dimensionality reduction method unraveled the BARDS spectral data by locating the salt samples in two-dimensional space with their distances and positions relative to their composition and crystalline structure. This study shows that BARDS data had a non-linear structure, which outperformed the manifold data visualization algorithms over linear ones. The projected BARDS data is capable of discriminating natural salts as well as different qualities of a certain product, hence its application as a low-cost quality control method was demonstrated in this study.

CRedit authorship contribution statement

Pedram Shoa: Conceptualization, Methodology, Validation, Formal analysis, Investigation, Data curation, Writing – original draft, Visualization. **Seyed Ahmad Mireei:** Supervision, Data curation, Writing – review & editing, Funding acquisition. **Abbas Hemmat:** Supervision, Writing – review & editing, Funding acquisition. **Sara W. Erasmus:** Methodology, Investigation, Writing – review & editing. **Saskia Van Ruth:** Supervision, Conceptualization, Methodology, Resources, Writing – review & editing, Project administration, Funding acquisition.

Declaration of Competing Interest

The authors declare that they have no known competing financial interests or personal relationships that could have appeared to influence the work reported in this paper.

Acknowledgments

The authors gratefully appreciate the financial support from Isfahan University of Technology (IUT), Isfahan, Iran and technical and equipment support from Wageningen University & Research (WUR), The Netherlands. The authors also would like to express their gratitude towards Eric Cuijpers, Erwin Brouwer, and Alex Koot for their valuable help and guidance.

References

- Anowar, F., Sadaoui, S., Selim, B., 2021. Conceptual and empirical comparison of dimensionality reduction algorithms (PCA, KPCA, LDA, MDS, SVD, LLE, ISOMAP, LE, ICA, t-SNE). *Comput. Sci. Rev.* 40, 100378.
- Bishop, C.M., 2006. *Pattern recognition. Mach. Learn.* 128.
- Crawford, F.S., 1982. The hot chocolate effect. *Am. J. Phys.* 50, 398–404. <https://doi.org/10.1119/1.13080>.
- Del Grosso, V.A., Mader, C.W., 1972. Speed of sound in pure water. *J. Acoust. Soc. Am.* 52, 1442–1446. <https://doi.org/10.1121/1.1913258>.
- Dupont, S., Ravet, T., Picard-Limpens, C., Frisson, C., 2013. Nonlinear dimensionality reduction approaches applied to music and textural sounds. 2013 IEEE Int. Conf. Multimed. Expo. (ICME) 1–6. <https://doi.org/10.1109/ICME.2013.6607550>.
- Fitzpatrick, D., Krüse, J., Vos, B., Foley, O., Gleeson, D., Ogormman, E., O'Keefe, R., 2012. Principles and applications of broadband acoustic resonance dissolution spectroscopy (BARDS): a sound approach for the analysis of compounds. *Anal. Chem.* 84, 2202–2210. <https://doi.org/10.1021/ac202509s>.
- Fitzpatrick, D., Evans-Hurson, R., Krüse, J., Vos, B., McSweeney, S., Casaubieilh, P., O'Gorman, É., 2013. The relationship between dissolution, gas oversaturation and outgassing of solutions determined by Broadband Acoustic Resonance Dissolution Spectroscopy (BARDS). *Analyst* 138, 5005–5010. <https://doi.org/10.1039/c3an36838f>.
- Galvis-Sánchez, A.C., Lopes, J.A., Delgado, I., Rangel, A.O.S.S., 2011. Fourier transform near-infrared spectroscopy application for sea salt quality evaluation. *J. Agric. Food Chem.* 59, 11109–11116. <https://doi.org/10.1021/jf202204d>.

- Galvis-Sánchez, A.C., Santos, I.C., Mesquita, R.B.R., Lopes, J.A., Rangel, A.O.S.S., Delgadillo, I., 2013. Application of mid- and near-infrared spectroscopy for the control and chemical evaluation of brine solutions and traditional sea salts. *Food Anal. Methods* 6, 470–480. <https://doi.org/10.1007/s12161-012-9458-7>.
- González, A., Armenta, S., de la Guardia, M., 2015. Mineral content of seasonings, salt and vinegar. In: *Handbook of Mineral Elements in Food*. John Wiley & Sons, Ltd, Chichester, UK, pp. 685–698. <https://doi.org/10.1002/9781118654316.ch30>.
- Guimet, F., Boqué, R., Ferré, J., 2006. Application of non-negative matrix factorization combined with Fisher's linear discriminant analysis for classification of olive oil excitation-emission fluorescence spectra. *Chemom. Intell. Lab. Syst.* 81, 94–106.
- Harris, C.R., Millman, K.J., van der Walt, S.J., Gommers, R., Virtanen, P., Cournapeau, D., Wieser, E., Taylor, J., Berg, S., Smith, N.J., 2020. Array programming with NumPy. *Nature* 585, 357–362.
- Hinton, G., Roweis, S.T., 2002. In: Citeseer, N.I.P.S. (Ed.), *Stochastic Neighbor Embedding*, pp. 833–840.
- Hwang, I.M., Yang, J.-S., Kim, S.H., Jamila, N., Khan, N., Kim, K.S., Seo, H.-Y., 2016. Elemental analysis of sea, rock, and bamboo salts by inductively coupled plasma-optical emission and mass spectrometry. *Anal. Lett.* 49, 2807–2821. <https://doi.org/10.1080/00032719.2016.1158831>.
- Karavoltos, S., Sakellari, A., Bakeas, E., Bekiaris, G., Plavšić, M., Proestos, C., Zinelis, S., Koukoulakis, K., Diakos, I., Dassenakis, M., Kalogeropoulos, N., 2020. Trace elements, polycyclic aromatic hydrocarbons, mineral composition, and FT-IR characterization of unrefined sea and rock salts: environmental interactions. *Environ. Sci. Pollut. Res.* 27, 10857–10868. <https://doi.org/10.1007/s11356-020-07670-2>.
- Lee, D.D., Seung, H.S., 1999. Learning the parts of objects by non-negative matrix factorization. *Nature* 401, 788–791.
- Lee, Y., Han, S.H., Nam, S.H., 2017. Soft Independent Modeling of Class Analogy (SIMCA) modeling of laser-induced plasma emission spectra of edible salts for accurate classification. *Appl. Spectrosc.* <https://doi.org/10.1177/0003702817697337>.
- Lee, Y., Ham, K.-S., Han, S.-H., Yoo, J., Jeong, S., 2014. Revealing discriminating power of the elements in edible sea salts: line-intensity correlation analysis from laser-induced plasma emission spectra. *Spectrochim. Acta Part B . Spectrosc.* 101, 57–67. <https://doi.org/10.1016/j.sab.2014.07.012>.
- Lee, Y., Nam, S.-H., Ham, K.-S., Gonzalez, J., Oropeza, D., Quarles, D., Yoo, J., Russo, R. E., 2016. Multivariate classification of edible salts: simultaneous laser-induced breakdown spectroscopy and laser-ablation inductively coupled plasma mass spectrometry analysis. *Spectrochim. Acta Part B . Spectrosc.* 118, 102–111. <https://doi.org/10.1016/j.sab.2016.02.019>.
- McInnes, L., Healy, J., Melville, J., 2018. Umap: Uniform manifold approximation and projection for dimension reduction. *arXiv Prepr. arXiv 1802, 03426*.
- NYQUIST, H., 1928. Certain topics in telegraph transmission theory. *Trans. Am. Inst. Electr. Eng.* 47, 617–644. <https://doi.org/10.1109/T-AIEE.1928.5055024>.
- Pagliarini, S., Schneider, S., Kello, C.T., Warlaumont, A.S., 2022. Low-dimensional representation of infant and adult vocalization acoustics. *arXiv Prepr. arXiv2204.12279*.
- Pedregosa, F., Varoquaux, G., Gramfort, A., Michel, V., Thirion, B., Grisel, O., Blondel, M., Prettenhofer, P., Weiss, R., Dubourg, V., 2011. Scikit-learn: machine learning in python. *J. Mach. Learn. Res.* 12, 2825–2830.
- van Ruth, S., Dekker, P., Brouwer, E., Rozijn, M., Erasmus, S., Fitzpatrick, D., 2019. The sound of salts by Broadband Acoustic Resonance Dissolution Spectroscopy. *Food Res. Int.* 116, 1047–1058. <https://doi.org/10.1016/j.foodres.2018.09.044>.
- Savitzky, A., Golay, M.J.E., 1964. Smoothing and differentiation of data by simplified least squares procedures. *Anal. Chem.* 36, 1627–1639. <https://doi.org/10.1021/ac60214a047>.
- Shoa, P., Ahmad Mireei, S., Hemmat, A., Erasmus, S.W., Van Ruth, S.M., 2021. Broadband acoustic resonance dissolution spectroscopy as a rapid tool for the compositional analysis of food powders: a case study of edible salts. *Food Chem.*, 129287 <https://doi.org/10.1016/j.foodchem.2021.129287>.
- Sorzano, C.O.S., Vargas, J., Montano, A.P., 2014. A survey of dimensionality reduction techniques. *arXiv Prepr. arXiv1403.2877*.
- Tan, M.M., Cui, S., Yoo, J., Han, S.H., Ham, K.S., Nam, S.H., Lee, Y., 2012. Feasibility of laser-induced breakdown spectroscopy (LIBS) for classification of sea salts. *Appl. Spectrosc.* <https://doi.org/10.1366/11-06379>.
- US Department of Commerce, N.O. and A.A., n.d. Why is the Ocean Salty?
- Van der Maaten, L., Hinton, G., 2008. Visualizing data using t-SNE. *J. Mach. Learn. Res.* 9.
- Wold, S., Esbensen, K., Geladi, P., 1987. Principal component analysis. *Chemom. Intell. Lab. Syst.* [https://doi.org/10.1016/0169-7439\(87\)80084-9](https://doi.org/10.1016/0169-7439(87)80084-9).
- Wu, D., Huang, Y., Chen, H., He, Y., Chen, S., 2017. VPPAW penetration monitoring based on fusion of visual and acoustic signals using t-SNE and DBN model. *Mater. Des.* 123, 1–14. <https://doi.org/10.1016/J.MATDES.2017.03.033>.